Compact in-vacuum switchable beam-dump system for radiation safety at accelerator beamlines

Sivaji Purushothaman,* Neeraj Kurichiyanil, and Ekaterina Kozlova
GSI Helmholtzzentrum für Schwerionenforschung, Planckstr. 1, 64291 Darmstadt, Germany

David J. Morrissey
Department of Chemistry, Michigan State University, East Lansing, Michigan 48824, USA

(Received 23 March 2026; accepted 27 July 2026; published 16 September 2026)

A compact, in-vacuum switchable beam dump is proposed as a first-of-a-kind engineering solution to improve operational flexibility in high-energy accelerator facilities. The design integrates beam-pass and beam-dump modes into a single wall-embedded unit, eliminating the need for external shielding and movable components outside the vacuum system. The concept is specifically developed for the superconducting fragment separator (Super-FRS) at Facility for Antiproton and Ion Research, making use of an existing opening in a modular radiation-shielding wall between experimental areas. It employs synchronous rotation to switch between an unobstructed vacuum beamline and a fully shielded beam-dump configuration. This architecture enables personnel access to downstream experimental areas while beam delivery continues in the upstream section. Two absorber configurations were investigated: an all-iron design and a mixed configuration incorporating the high-density tungsten alloy Densimet. Iron provides cost-effective bulk shielding and strong attenuation of secondary gamma radiation, whereas Densimet enables compact energy deposition with superior stopping power. The required thickness of additional downstream boron carbide shielding to adequately suppress slow neutrons differs between the two options. FLUKA Monte Carlo simulations confirm that both configurations satisfy the stringent personnel safety limit of $< 3\ \mu\mathrm{Sv/h}$ in all relevant scenarios. Complementary vacuum simulations demonstrate that the beamline pressure remains below 5×10^{-6} mbar during operation. The results indicate that the proposed switchable beam dump offers a viable path to enhance facility availability and throughput at Super-FRS. The compact, modular concept is scalable and may be adapted to other high-energy accelerator facilities facing similar space and access constraints.

DOI: 10.1103/58pd-c2yb

I. INTRODUCTION

Beam-intercepting systems are essential components of accelerator facilities to absorb or control the energy and power of charged-particle beams. They can be classified into three categories based on their operational purpose: (i) particle-producing devices, such as production targets or reaction targets; (ii) beam-conditioning systems, including collimators and scrapers for beam shaping, cleaning, or halo reduction; and (iii) radiation-safety systems, such as beam dumps or stoppers that terminate propagation of the beam. Conventional beam-intercepting elements, such as the stoppers in CERN's injector complex [1], primarily serve as safety devices to prevent beam propagation during abnormal or emergency conditions. In contrast, beam dumps are dedicated systems designed to absorb the full beam energy in a controlled manner during normal operation or at the end of a beam cycle and are typically implemented as static installations.

High-energy facilities must balance the demand for high scientific throughput with stringent radiation-safety protocols and limited experimental floor space. Existing movable devices for beam interception, like the scrapers, collimators, beam stoppers, or rotating absorbers found in systems with high-power targets, typically intercept only a portion of the beam or distribute thermal loads [1–4] and do not offer a fully shielding configuration. Transfer line external dumps (TEDs), as used in the Super Proton Synchrotron to Large Hadron Collider lines at CERN, represent a more relevant precedent [5,6]. These insert an absorber transversely into the beam path via Y-shaped vacuum chambers, with the drive mechanism largely outside the vacuum, giving fast insertion and retraction. Such a concept inherently presents a retraction pocket in the

*Contact author: S.Purushothaman@gsi.de

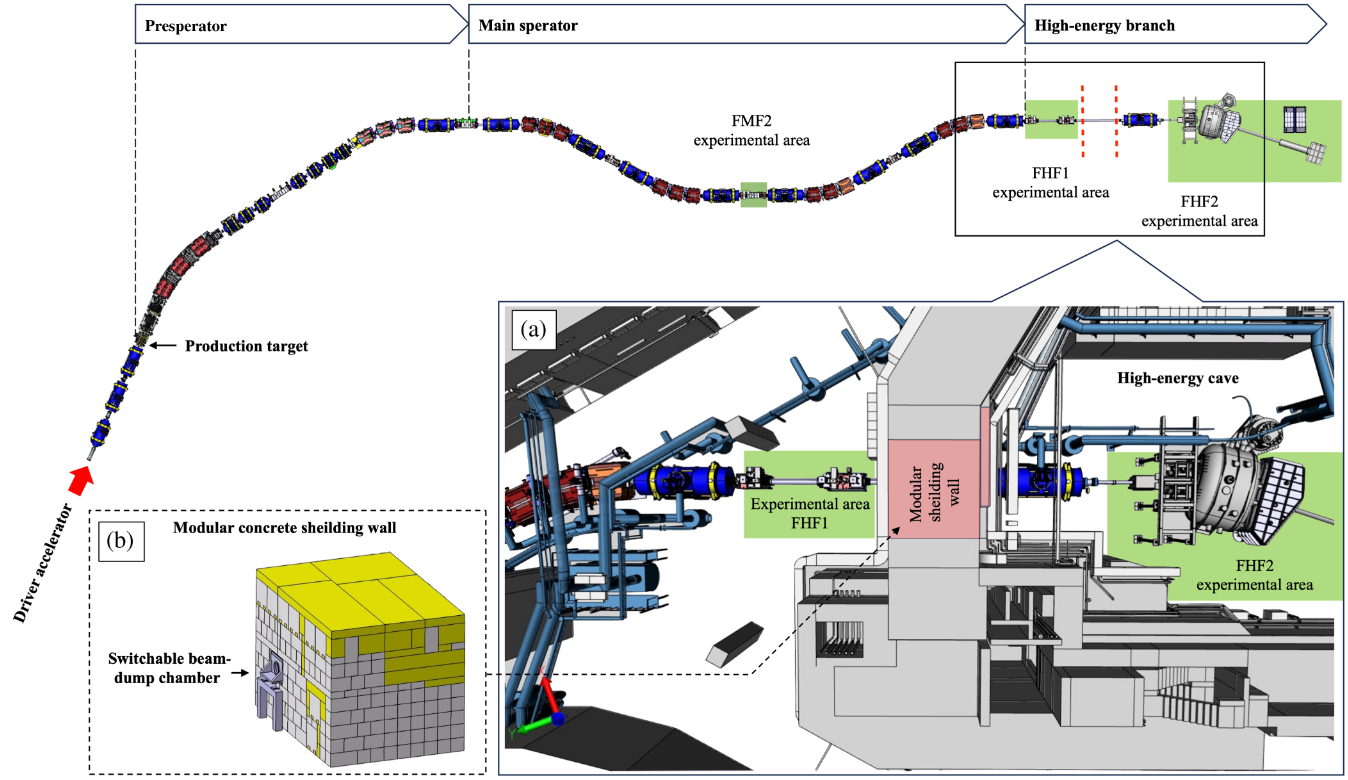

FIG. 1. Layout of the superconducting fragment separator (Super-FRS) in the early- and first-science configuration. Green-shaded regions indicate experimental areas at dedicated focal planes. In the high-energy branch (inset a), the experimental areas FHF1 (in the tunnel) and FHF2 (in the High-Energy Cave) are separated by a 5.7-m-thick modular concrete shielding wall. This shielding wall (inset b) includes a rectangular opening of 1.12×1.00 m to accommodate the vacuum beamline connection between the two sections.

beam-pass state, which would create a shielding discontinuity and a streaming path for secondary radiation, particularly fast neutrons and muons, within an envelope that cannot accommodate additional compensating shielding.

The conceptual design presented here assesses the technical feasibility of a compact, wall-integrated beam dump capable of fast switching between *beam-pass* and *beam-dump* operational states. Fully contained in a vacuum vessel, the assembly supports direct coupling to the accelerator beamline vacuum or operation in atmospheric conditions. This approach minimizes the physical footprint within the facility and increases research productivity by shortening the time needed to reconfigure shielding between experimental campaigns. To the best of our knowledge, this is the first system to integrate a full-shielding beam-dump and beam-pass functionality into a compact, wall-embedded vacuum assembly. This novel design allows safe downstream personnel access while the upstream beam remains operational.

The superconducting in-flight fragment separator Super-FRS [7] at the Facility for Antiproton and Ion Research (FAIR) in Darmstadt, Germany, provides a particularly important application for such a system due to its staged operational schedule. The early science (ES) phase of FAIR will begin the operation of Super-FRS using beams from the existing Schwerionensynchrotron (heavy-ion synchrotron)-18 synchrotron [8] for the initial nuclear structure astrophysics and reactions (NUSTAR) collaboration experiments [9]. Subsequently, the first science (FS) and first science plus (FS+) phases will employ the high-power Schwerionensynchrotron (heavy-ion synchrotron)-100 synchrotron to deliver beams for the core NUSTAR and Compressed Baryonic Matter (CBM) programs. During the ES and FS phases, the Super-FRS will deliver high-intensity heavy-ion beams to the experimental areas located at three of its focal planes: the midfocal plane (FMF2) and the two high-energy branch focal planes: FHF1 in the tunnel and FHF2 in the high-energy cave. Figure 1 illustrates the Super-FRS layout during the ES and FS phases, highlighting the experimental areas at FHF1 and in the high-energy cave. Given the limited number of active beamlines in the initial stages of FAIR operation, efficient infrastructure utilization must be ensured by allowing controlled personnel access to the high-energy cave for experimental preparation during beam operations at FHF1. This operational requirement necessitates intercepting the beam between FHF1 and the high-energy cave.

Conventional static beam-dump solutions, such as a mobile shielding block with dimensions of approximately $1 \times 1 \times 2$ m placed in the FHF1 area, would not only occupy valuable experimental space but also be impractical due to the frequent removal required during the commissioning phase of the Super-FRS and the R^3B setup in the high-energy cave. In addition, radiation-safety constraints associated with the handling, transportation, and storage of large-scale activated materials would further complicate their use. The design presented here addresses these limitations by utilizing the aperture in the modular shielding wall intended for the interconnecting beam pipe. Key advantages of this concept include: (i) Fast switching between beam-pass and beam-dump modes while reducing the floor space required compared to a conventional static beam dump. (ii) During the transition from beam-dump mode to beam-pass mode, the irradiated surface of the primary absorber block is rotated by 90° and enclosed within the shielding structure, preventing direct exposure of personnel to activated surfaces and reducing residual radiation exposure during access.

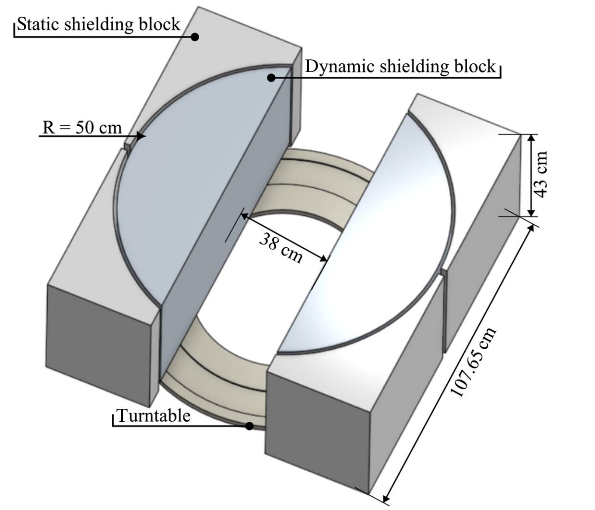

FIG. 2. Conceptual model of a single shielding unit. Two dynamic shielding blocks are surrounded by four static shielding blocks. The turntable allows 90° rotation of the dynamic blocks about the central axis.

II. SYSTEM CONCEPT, MECHANICAL DESIGN, AND INTEGRATION

The design of the switchable beam dump presented here is tailored to the dimensional and operational constraints of the Super-FRS FHF1 area, the high-energy cave, and the modular shielding wall separating them (see Fig. 1). The assembly in its vacuum chamber is engineered to fit a predefined physical aperture of $1.12 \times 1.00 \times 5.70$ m in the wall. Given its classification as radiation-safety-relevant, the mechanical design prioritizes structural robustness, long-term shielding reliability, and operational stability under sustained irradiation. Vacuum compatibility is ensured by careful choice and pretreatment of materials in a vacuum with optimization of molecular flow conductance for an even distribution of residual gas pressure along the system. Beyond standard vacuum hardware, the chamber includes dedicated ports for drive mechanisms, diagnostic feed-throughs, and safety-critical instrumentation.

A. Rotating shielding concept

The core of the system comprises five shielding units. Each unit consists of a pair of coaxially mounted identical plano-convex cylindrical segments (hereinafter referred to as *dynamic shielding blocks*). The geometry of each segment is derived from a right circular cylinder partitioned by an offset plane parallel to its longitudinal axis. The flat faces of each segment are oriented inward, forming a continuous rectangular slot that spans the full length of the unit.

The dynamic shielding blocks are each mounted on an independent turntable and surrounded by four *static shielding blocks* configured to complete a rectangular shielding geometry, as illustrated in Fig. 2. While the nominal Super-FRS beam aperture is 38×38 cm, the system provides a total vertical clearance of 43 cm. This additional 5 cm margin is an allowance for potential long-term structural settling of the facility relative to the beam axis. The five shielding units and their associated turntable mechanisms are installed inside a vacuum chamber with internal dimensions of $0.96 \times 1.08 \times 5.70$ m. The transition between beam-pass and beam-dump modes is achieved by synchronously rotating the dynamic shielding blocks by 90°, as illustrated in Fig. 3.

Material selection for the system components focused on radiation-safety requirements, cost-efficiency, vacuum compatibility, and long-term maintainability [10–12]. Stainless steel with reduced concentrations of alloying elements such as chromium (Cr), nickel (Ni), manganese (Mn), and trace cobalt (Co), known contributors to long-term activation in high-energy accelerator environments [12,13], is considered for the vacuum chamber and

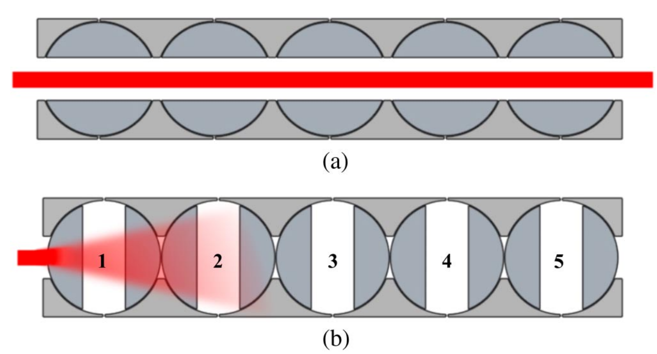

FIG. 3. Top-view schematic illustrating the two operational modes of a switchable beam-dump system with five shielding units. The beam is shown in red and propagates from left to right. (a) Beam-pass mode, in which the apertures in the shielding units are aligned to let the beam transmit through the system. (b) Beam-dump mode, where 90° rotation of the dynamic shielding blocks intercepts the beam.

TABLE I. Key physical parameters of the switchable beam-dump system considered in the present study.

Average shielding thickness per unit	58 cm
Total number of shielding units	5
Open aperture (beam-pass mode)	43×38 cm
Shielding thickness (beam-dump mode)	2.9 m
Weight of one shielding unit (see Fig. 2)	
Iron	2.48 t
Densimet	5.83 t
Weight of two dynamic shielding blocks (see Fig. 2)	
Iron	1.40 t
Densimet	3.29 t

interface elements due to its vacuum compatibility, corrosion resistance, and mechanical reliability. Materials considered for the shielding units are the tungsten alloy Densimet® (97% W, 2% Ni, and 1% Fe) and pure iron (Fe). Additional boron carbide (B_4C) shielding was placed externally on the downstream side to enhance neutron attenuation [14]. Overall, this material selection supports effective shielding and safer maintenance and decommissioning in accordance with as low as reasonably achievable (ALARA) radiation-protection principles [13]. The physical parameters of the system are summarized in Table I with the selected materials and geometry.

B. Mode switching mechanism

Switching between beam-dump and beam-pass modes requires synchronized rotation of all the dynamic shielding blocks by 90° within the vacuum chamber. Two possible mechanical synchronization concepts are shown in Fig. 4. Either a gear-based configuration using a cascade of intermeshing spur gears or an alternating linkage configuration employing rigid coupling rods can ensure reliable, simultaneous rotation of all of the dynamic shielding blocks. The alternating linkage design was considered less suitable due to the added complexity associated with the gaps introduced in the beam direction by the moving rods and was therefore excluded from detailed consideration in the current work. Both motorized and manual operation modes are possible, the latter exclusively for servicing and maintenance purposes. Manual intervention is only foreseen under controlled-access conditions, after beam shutdown and with residual dose rates verified to be within acceptable limits in accordance with the applicable radiation-protection procedures of the facility. The switching motion is intended to be executed over a time scale of several tens of minutes in order to limit angular acceleration, reduce inertial loads, and avoid transient torque peaks during start-up and braking. This controlled motion minimizes mechanical stress on the bearings, shafts, and synchronization components.

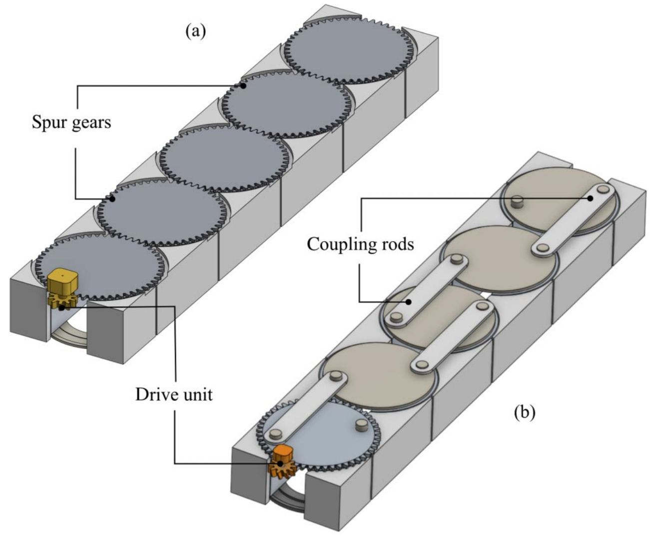

FIG. 4. Conceptual designs for the shielding rotation mechanism driven by a single motorized drive unit. (a) Gear-based synchronization using a series of spur gears and (b) alternative linkage synchronization using coupling rods.

The shielding blocks absorb the beam power during dump operation; however, as shown in Sec. V, the deposited power levels are sufficiently low that thermal expansion of the rotating blocks and gear train remains within acceptable mechanical tolerances.

Since the mechanism operates in vacuum, conventional liquid or grease lubricants are undesirable due to outgassing, radiation-induced degradation, and radiolytic gas production. Dry-running or solid-lubricated ultrahigh vacuum-compatible components are therefore foreseen, such as metallic or ceramic bearing systems with radiation-tolerant solid lubricant coatings [15–17]. All candidate solutions will require qualification under the expected radiation environment, and the final selection will be made during detailed engineering in line with ultrahigh vacuum, radiation, and maintenance requirements. The tribological demands are modest: fewer than approximately 20 transitions per year under slow, quasi-static motion, with reliable positioning and long-term vacuum compatibility as the primary requirements rather than high-cycle or high-speed performance.

C. Installation, alignment, and serviceability

The switchable beam dump is contained within a vacuum chamber that is structurally decoupled from the surrounding shielding wall. During installation and positioning of the chamber on its base support, one side of the modular shielding wall will remain open to provide lateral access. After alignment, the chamber will be embedded in the fully closed modular wall. All auxiliary components necessary for the switching mechanism, such as the motor unit and position sensors, the vacuum components, and other feed-throughs, will be in accessible locations and mountable after the integration of the vacuum chamber into the modular wall.

Although routine removal of the complete system is not foreseen, an integrated rail or sliding mechanism can be used to enable the chamber to be withdrawn horizontally from its embedded position without dismantling the surrounding shielding. Given the substantial mass of the assembly, the rail or sliding interfaces must be designed to relieve static contact loads in order to prevent surface galling or cold welding at the contact areas. This can be achieved by transferring the system weight to adjustable leveling supports, which also enable precise beam-axis alignment and any compensation needed for long-term structural settling.

The interfaces between the chamber and the upstream and downstream beamlines use slidable adapters with ethylene propylene diene monomer elastomer seals to accommodate installation tolerances and any beamline alignment offsets. These interfaces also allow compensation for potential structural settling without inducing mechanical stress in the vacuum boundary.

III. OPERATIONAL STATES AND SAFETY INTERLOCK INTEGRATION

Beam operations with high-intensity heavy-ion beams, specifically up to 1 GeV/u and intensities exceeding 10^7 particles/s, demand exceptionally stringent radiation-protection measures. According to the German Radiation Protection Ordinance [18], controlled access is only permissible when local ambient dose-equivalent rates remain below 3 μSv/h, corresponding to the definition of a *controlled area*. Areas with local dose rates above this threshold are classified as *inaccessible areas* and may not be entered. Both controlled and inaccessible areas are always clearly marked with barriers, closed doors, and radiation warning signs. The existing GSI internal access regulations align with these legal requirements, ensuring that personnel access is only possible when dose-rate conditions meet the controlled-area criteria.

To satisfy these operational and legal constraints, the switchable beam-dump system operates in two mutually exclusive states: *beam pass* and *beam dump*. These states are intended to be integrated into the FAIR personnel access safety (PAS) system and the machine-interlock architecture of the Super-FRS. The safety concept follows the layered radiation-protection philosophy commonly adopted at high-energy accelerator facilities [19] that combines passive shielding with active access-control and machine-protection systems.

Within this framework, the beam-dump assembly functions conceptually both as a radiation-safety barrier and as a machine-permit element within the interlock logic. The final control-system implementation will therefore be required to meet performance level e (PL e) according to EN ISO 13849-1 [20] and to follow the functional-safety principles of IEC 61508 [21]. Although a detailed safety-control architecture is beyond the scope of this conceptual design study, the concept assumes redundant position verification, mechanical locking confirmation, and fail-safe interlock logic to prevent unintended beam transmission under fault conditions.

In *beam-pass* mode, the system functions as a standard vacuum beamline section, allowing unobstructed beam passage to the downstream experimental area. In this configuration, the PAS would register an unsafe state prohibiting personnel access to both upstream and downstream regions. In *beam-dump* mode, the dynamic shielding elements are rotated into position to intercept the beam upstream of the high-energy cave. Once all beam-blocking elements are fully inserted, mechanically locked, and verified through redundant safety channels, the PAS would transition to a safe state, allowing controlled personnel access to the downstream experimental area while the upstream region remains radiation controlled.

From the machine-protection perspective, beam operation would be permitted only when the system is verified to be in one of the two mechanically secured states. Any undefined intermediate position would immediately trigger a beam inhibit, preventing beam transport under unsafe or uncertain conditions.

The system must satisfy three principal design requirements: (i) a prompt dose rate below 3 μSv/h in the downstream experimental area during beam-dump operation; (ii) residual dose rates permitting controlled personnel access to the upstream area within approximately 1 week of beam-off; and (iii) beamline-compatible vacuum pressure below 5×10^{-6} mbar during operation, where uninterrupted beam transport to downstream users must be preserved. Vacuum requirements in beam-dump mode are relaxed accordingly since downstream transport is intentionally interrupted. The FLUKA and vacuum simulations presented in the following sections demonstrate that both absorber configurations satisfy all three criteria with substantial margin.

IV. RADIATION SAFETY ANALYSIS

Two configurations of the switchable beam-dump materials were evaluated in the radiation-safety simulations, as summarized in Table II. In Case 1, all five shielding units were made of pure Fe (density 7.874 g/cm^3). In Case 2, the first shielding unit in the beam direction was replaced by Densimet (density 18.5 g/cm^3), while the remaining four units were made of pure Fe. In both configurations, additional shielding blocks made of boron carbide (B_4C, density 2.52 g/cm^3) were placed downstream of the last shielding unit to absorb slow neutrons. The shape and thickness of these blocks differ between the two cases (see Appendix A). Accounting for the tolerances for installation, a gap of at least 2 cm would be required between the switchable beam-dump system and the concrete shielding wall. However, as a

TABLE II. Shielding configurations used in the radiation-safety simulations. The numbering of the shielding units is indicated in Fig. 3. Additional downstream B_4C blocks were included to provide external shielding in both cases.

Configuration	Unit number and material composition	Weight (t)
Case 1	(1–5) Fe	12.4
Case 2	(1) Densimet, (2–5) Fe	15.8

conservative value, the simulations included 5 cm unshielded gaps.

The Monte Carlo (MC) code FLUKA [22–24] (version 2025.1.3) was used to perform the radiation-protection calculations. FLAIR [25] was used to reproduce the concrete shielding wall (2.3 g/cm^3), experimental areas, and switchable beam dump for the calculations in a simplified geometric configuration (see Appendix A). The beam source was modeled as a rectangular-shaped (20×10 cm) beam of ^{208}Pb nuclei with a kinetic energy of 1 GeV/u and an intensity of 1×10^7 particles/s. The simulation transported all particles until they were captured or ranged out, accounting for the full description of hadronic and electromagnetic cascades. For hadrons, the transport threshold was set to 100 keV, except for neutrons, which were followed down to thermal energies. Electrons, positrons, and photons were transported by activating the FLUKA electromagnetic transport option. The full transport of all light and heavy ions (including nuclear interactions) was enabled by default. A region-based importance-biasing particle-splitting algorithm was applied to all particles transported through concrete shielding and beam dump. Dose rates were calculated using fluence-to-dose conversion factors from Refs. [13,26], as implemented in the code. The geometry in the simulation is arranged such that $(x = 0, y = 200)$ represents the beam axis. The beam is generated at $z = 0$ and travels in $+z$ direction. The switchable beam dump and modular concrete wall begin at $z = 90$ cm and end at $z = 690$ cm. The FHF1 experimental area extends downstream from $z = 90$ cm in $-z$ direction, and FHF2 (high-energy cave) starts from $z = 690$ cm in $+z$ direction.

Two operational scenarios are of particular interest in this study. (i) First, when the beam is intercepted by the beam-dump system, the shielding must ensure sufficiently low dose rates in the downstream high-energy cave to allow controlled personnel access. (ii) Second, after the beam-dump operation and the machine being switched off, the residual dose in the upstream FHF1 experimental area should decrease to levels permitting personnel access within a reasonably short cooling-off period. Practically, in scenario (i), a dose rate lower than 3 μSv/h is desirable in the cave. In scenario (ii), a cooling-off time less than 1 week is strongly desired. Simulation results showing the prompt dose-rate distributions for Case 1 and Case 2 are shown in Fig. 5. It can be seen that, under all considered configurations, the beam dump ensures compliance with radiation-safety limits. The calculated dose rates in the FHF2 high-energy cave remain well below the 3 μSv/h controlled-access threshold.

Residual dose rates were simulated assuming continuous beam-dumping operation with the same beam parameters for a period of 30 days followed by cooling-off times of 1 day, 1 week, and 1 month. Figure 6 shows the simulated residual dose rates for a rather pessimistic configuration, where the dynamic shielding unit that primarily intercepts the beam is directed toward the experimental area. For a 1 GeV/u ^{208}Pb beam, the primary-ion stopping depth is approximately 17 mm in iron and 9 mm in tungsten (Densimet contains ∼97 wt.% tungsten). The strongest local activation occurs near the end-of-range (Bragg-peak) region, which lies much shallower in Densimet. Counterintuitively, Case 2 (Densimet) exhibits overall lower residual dose rates and a faster decay with cooling time than Case 1 (iron).

Although the heavier tungsten content in Densimet results in higher secondary fragment production and shifts the center of mass of residual nuclei production shallower into the material, its superior density provides significantly higher attenuation of gamma rays. The material thus effectively self-shields its own residual radiation, lowering dose rates outside the beam-dump region.

Specifically, the mean energy of the gamma flux from radionuclides produced in iron is approximately 1.3 MeV, whereas in tungsten, it drops to about 0.8 MeV (only isotopes contributing $\geq 1\%$ to the total dose are considered; see Appendix C). Using mass attenuation coefficients from the NIST XCOM database [27] (5.35×10^{-2} cm^2/g for iron at 1.25 MeV and 8.07×10^{-2} cm^2/g for tungsten at 0.8 MeV), the corresponding tenth-value layers (TVLs) are approximately 5.5 and 1.5 cm, respectively. Together with the half-lives of the dominant radionuclides produced in tungsten and iron (see Appendix C), this explains the lower dose and the faster decrease in dose observed in Case 2, as shown in Figs. 6 and 7. For the simulation, iron was used as a surrogate for stainless steel, as it is planned to use a material with a low content of alloying elements. The study performed here [10] indicates that the main contributors to the dose rate are ^{54}Mn, ^{52}Mn, ^{48}V, and ^{48}Sc, which are primarily produced from iron rather than from the alloying elements. Furthermore, the benchmark study presented in Ref. [28] demonstrates that FLUKA reproduces the measured specific activities very well. Therefore, the assumption of using pure iron in the simulation is reasonable, since the dominant contributors to the dose rate originate primarily from iron rather than from the alloying elements.

While secondary fragments and neutron-induced reactions can spread residual activation somewhat beyond the primary-ion range, the dominant contribution remains

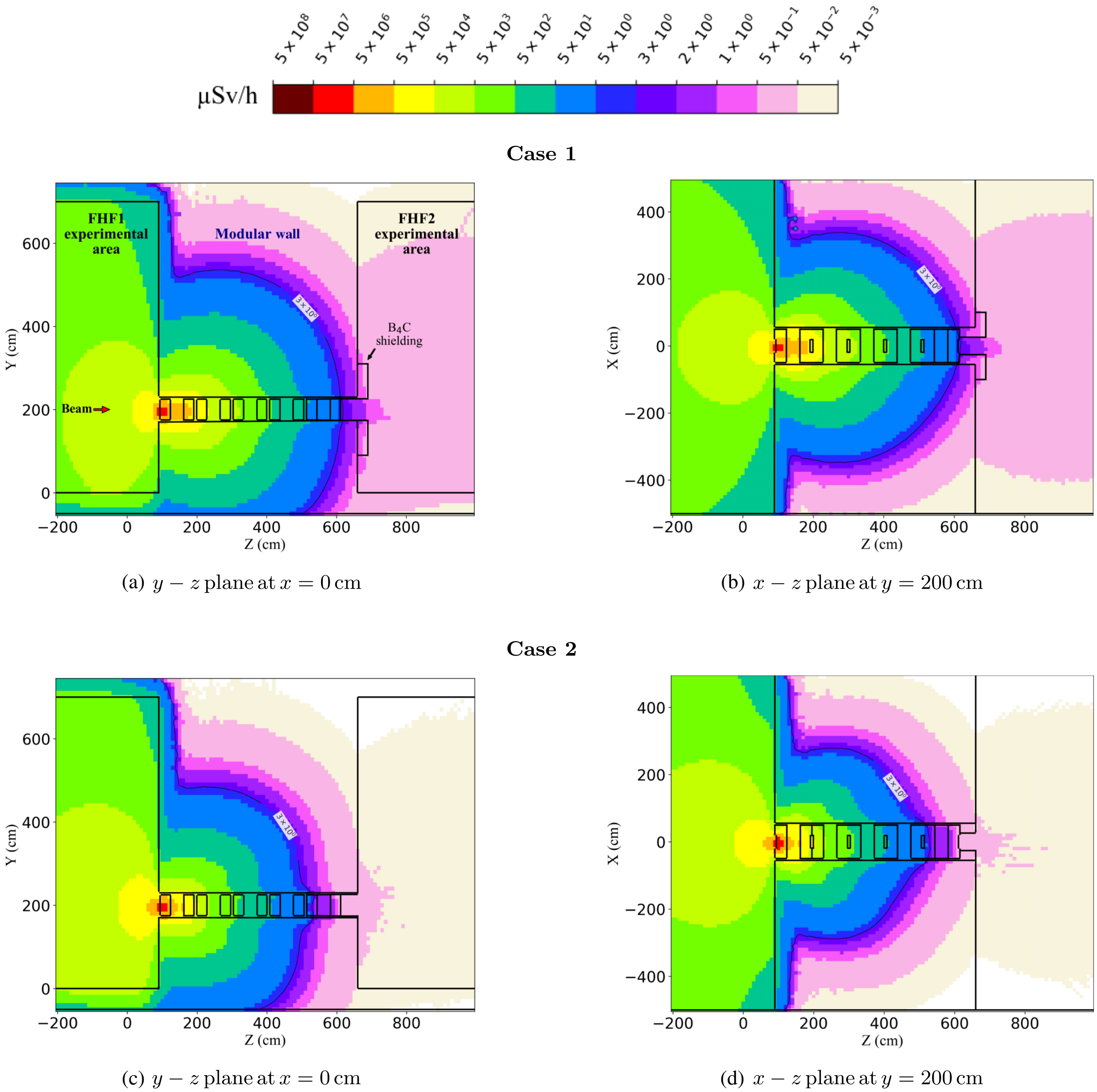

FIG. 5. Calculated prompt dose-rate distributions produced during beam-dump operation in the switchable beam-dump system. Panels (a) and (c) show the side view ($y-z$ plane at $x=0$), while panels (b) and (d) show the top view ($x-z$ plane at $y=200$ cm). The top row corresponds to Case 1 and the bottom row to Case 2; see the text. The statistical uncertainty of the calculation is less than 10%.

localized near the stopping region. In the actual operating configuration, rotating the dynamic shielding unit by 90° to beam-pass mode fully encapsulates the activated surfaces within the surrounding static shielding blocks. As a result, residual radiation levels in the FHF1 area are expected to be significantly lower than the conservative estimates provided by the simulations, where the primary absorber faces the experimental area.

Figure 7 summarizes the simulation results for both prompt and residual radiation studies, illustrating the dose-rate profiles evaluated along the longitudinal axes $(x=0,z)$ and $(x=200,z)$ within the $y=200$ cm plane. For the prompt-radiation field [Fig. 7(a)], both absorber configurations demonstrate a rapid, exponential decrease in dose-rate downstream of the beam dump. Crucially, the ambient dose-equivalent rates in the high-energy cave remain well below the controlled-area threshold of 3 μSv/h. The configuration utilizing the Densimet-based unit (Case 2) exhibits slightly stronger attenuation near the interaction region due to its higher material density and

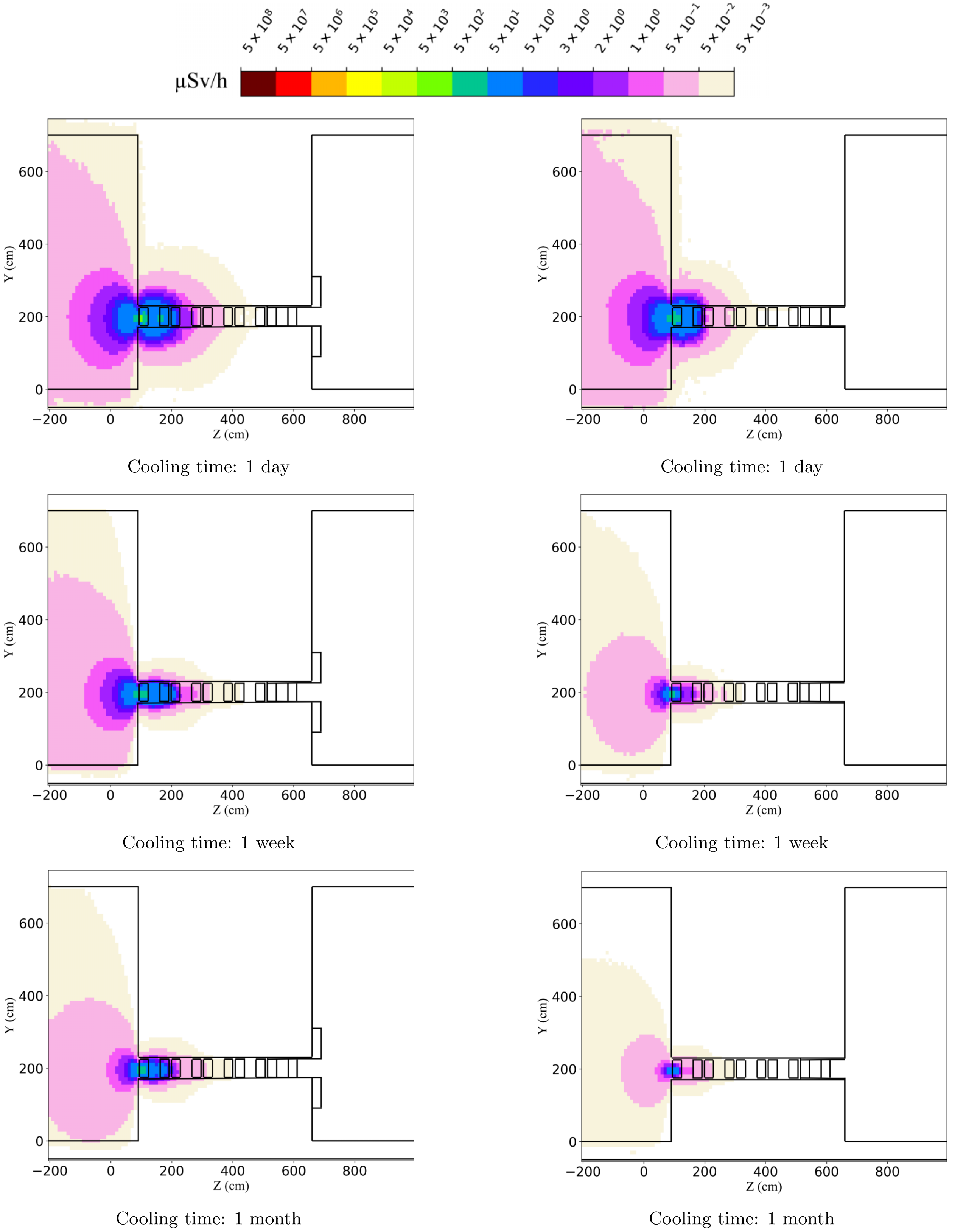

FIG. 6. Residual dose-rate distributions for two shielding configurations of the switchable beam-dump system: Case 1 (left) and Case 2 (right). Only the side view ($y-z$ plane at $x=0$) is shown. The ambient dose-equivalent rate (μSv/h) is displayed on a logarithmic scale for cooling times of 1 day, 1 week, and 1 month. The top-left panel illustrates the configuration of the experimental areas and the modular shielding wall. The statistical uncertainty of the calculation is less than 10%.

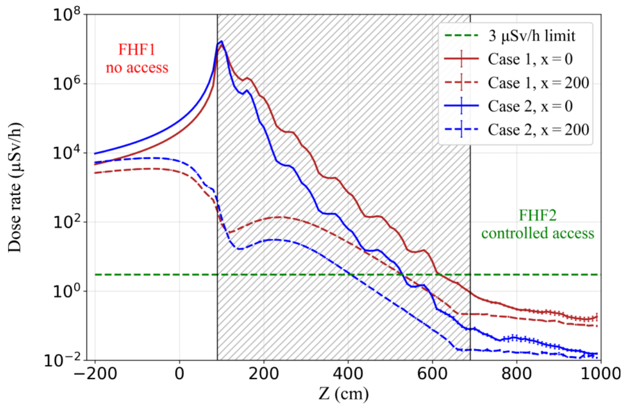

(a) Prompt dose rates

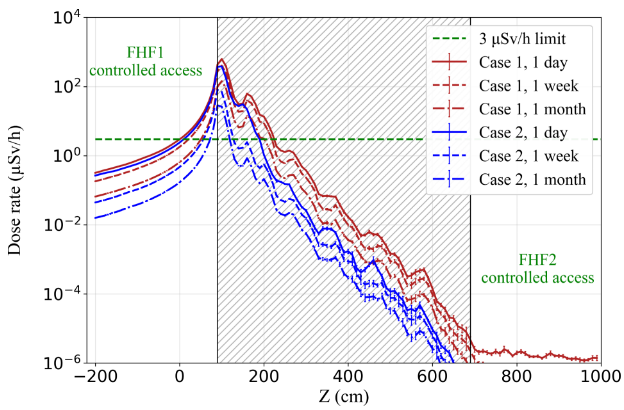

(b) Residual dose rates

FIG. 7. Comparison of prompt and residual dose-rate profiles along the beam axis for Case 1 and Case 2. Panel (a) shows prompt dose rates and panel (b) residual dose rates. The hatched region represents the modular concrete shielding wall. The dotted green line represents the 3 μSv/h access limit. The radiation-safety status of the experimental areas is indicated.

stopping power. At larger distances, however, the difference between the two configurations becomes negligible, indicating that the overall macroscopic shielding thickness dominates the attenuation of the prompt-radiation field.

Regarding activation, the residual dose distributions [Fig. 7(b)] reveal a strong reduction with increasing cooling time. One day postirradiation, access to the FHF1 area becomes radiologically permissible starting 90 cm upstream of the first shielding unit. After approximately 1 week of cooling, dose rates in the upstream experimental area approach the controlled-access limit, and after 1 month, they drop to negligible levels.

These calculations demonstrate that the conceptual design provides a substantial safety margin for a 1 GeV/u ^{208}Pb beam at 10^7 particles/s, with effective containment of radiation within the shielding envelope. Although the Densimet configuration (Case 2) offers the highest shielding performance, its substantially higher material and machining costs compared with iron, together with the increased mass (15.8 versus 12.4 t, see Table I), present significant challenges for mechanical design, integration, and handling. Reinforced supports, higher actuation torque, specialized lifting procedures, and tighter alignment tolerances would all be required.

To enable immediate access to the experimental area, commercially available configurable mobile lead shielding systems can be deployed. These compact units, consisting of overlapping lead mats on mobile frames, can be positioned locally to attenuate residual activity without adding appreciable space (see Appendix B).

For future detailed validation of additional shielding states, scripted geometry variations in FLUKA, combined with activation-analysis workflows such as DORIAN [29], could be used to systematically evaluate alternative shielding configurations, activated-component replacement scenarios, and maintenance conditions.

V. THERMAL CONSIDERATIONS

The thermal impact of the primary beam was evaluated to assess the system's overall thermal stability. Assuming a continuous (dc) beam delivery with an intensity of 10^7 ions/s, the total deposited beam power is only 0.33 W. Even under the conservative assumption that all of this energy is deposited exclusively within the first dynamic shielding block segment (a mass of 700 kg; see Table I) with zero heat dissipation to represent the absolute worst-case scenario, the thermal impact remains extremely low, resulting in a negligible bulk temperature increase of approximately 1.05×10^{-6} K/s (< 0.004 K/h).

In practice, since the thermal load is negligible, the generated heat can dissipate passively into the surrounding static shielding and the vacuum-chamber walls, eliminating the need for active cooling. This inherent thermal stability ensures there is no impact on the mechanical tolerances, preserving the simplicity and reliability of the in-vacuum rotational mechanism.

VI. VACUUM SYSTEM CONCEPT

Any system to be integrated into the accelerator beamline must also satisfy the vacuum requirements of the machine. The Super-FRS, being a single-pass machine for high-energy heavy ions, requires only a moderately high vacuum between 5×10^{-6} and 5×10^{-7} mbar (1 mbar $= 10^2$ Pa) during the beam transport and experiments. Obtaining a good vacuum in such large and complex systems begins with the material selection for lower surface outgassing, sealing concepts for low leak rates and permeation, structural integration, conductance optimization for minimizing obstruction to molecular gas flow, and by following standard guidelines on vacuum system cleaning and handling to avoid contamination. To maintain long-term vacuum integrity, the chamber design utilizes metallic seals, as opposed to rubber O-rings conventionally applied to systems of this scale, in all radiation-exposed as well as permanently inaccessible regions.

For systems with restricted and dynamic conductance, analytical calculations only provide poor estimates of vacuum pressures, and MC simulations in the molecular flow regime are better suited to make reliable estimates. Therefore, a model of the system was simulated using the MC code MolFlow+ [30] (v2.10.0) with a simplified geometry that contained all of the relevant vacuum-exposed surfaces and volumes, as shown in Fig. 8(a). The simulations were carried out with 5×10^5 desorption events (approximately 5×10^6 surface hits) until statistically stable pressure estimates were obtained. To evaluate the effect of different overall molecular flow conductance between beam-pass and beam-dump modes, geometrical configurations representing these states were separately simulated. Additionally, for each configuration, both the ideal pumping configuration and a failure scenario were separately simulated to evaluate operational vacuum robustness. In beam-pass mode, specific outgassing rates typical for conditioned stainless steel (5×10^{-10} mbarls^{-1} cm^{-2}) and iron shielding components (5×10^{-9} mbarls^{-1} cm^{-2}) were assumed. The specific outgassing rate quantifies the amount of gas released from a material per unit surface area per unit time. For beam-dump mode, beam-induced desorption was conservatively estimated to increase the effective outgassing rates of all the surfaces by 1 order of magnitude. Under static conditions, for the given volume, materials, and exposed surface area, a pressure below 5×10^{-6} mbar can be achieved using two 9501 s^{-1} TMPs placed at both ends of the chamber to provide the required symmetric pressure distribution.

Figure 8b shows the results of the vacuum simulations. A symmetric distribution of pressure was obtained with the dual pumping arrangement, reaching pressures of 1.60×10^{-6} and 2.60×10^{-6} mbar in beam-pass and beam-dump modes, respectively. When only a single pump is present, an increased and asymmetric distribution of pressure can be expected, with values peaking at 3.30×10^{-5} and 7.10×10^{-5} mbar for beam-pass and beam-dump cases, respectively. These results demonstrate that this conceptual design satisfies the vacuum requirements in beam-pass mode, including under single-pump operation. In beam-dump mode, the higher pressure levels remain acceptable since downstream beam transport is intentionally interrupted. As part of the design study, additional operational configurations were considered in which the beam is dumped under reduced vacuum or atmospheric conditions on demand by upstream experiments. Since beam-dump mode does not require downstream beam transport, the chamber can be isolated from the machine vacuum using a thin separation window if required. Isolation valves in front of the TMPs would allow decoupling them from the accelerator vacuum system. In this configuration, rough vacuum ($< 10^{-1}$ mbar) could be maintained using bypassed backing pumps. Full atmospheric operation is likewise feasible by venting the chamber and isolating high-vacuum components.

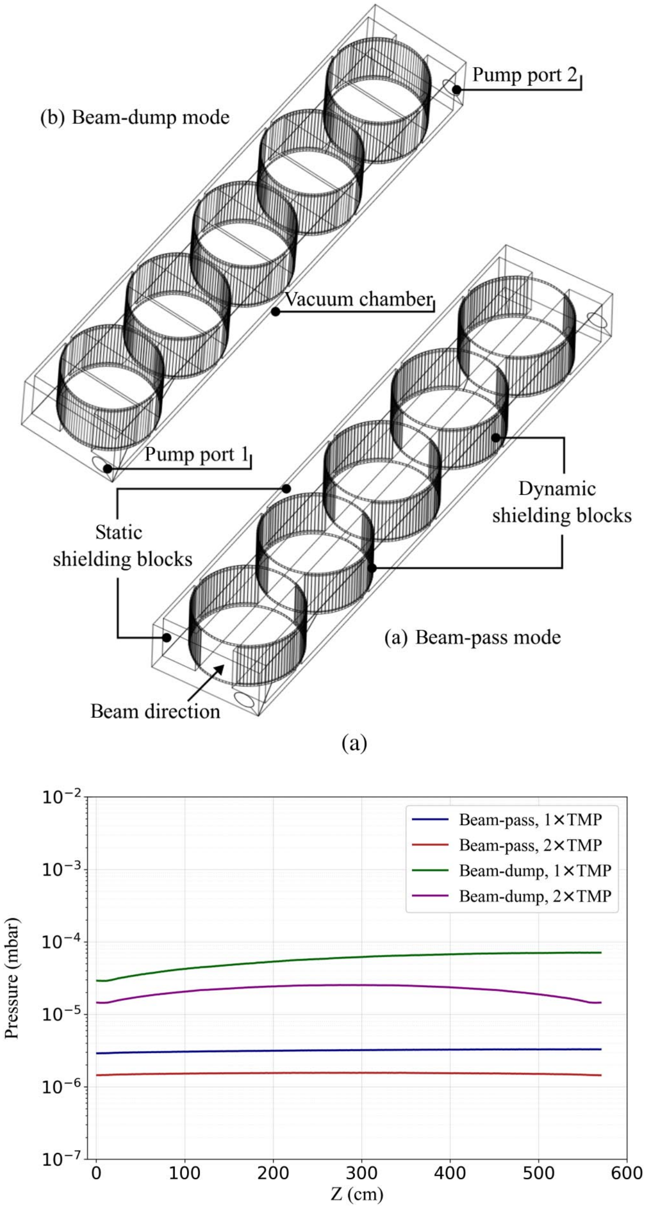

FIG. 8. Monte Carlo simulation results for the switchable beam-dump vacuum system: (a) Simplified geometries used in the simulation model and (b) calculated pressure distributions along the chamber. Results are shown for both beam-pass and beam-dump modes with two turbo molecular pumps (TMPs) running as in the ideal pumping setup ($2 \times$ TMP), as well as for the failure scenarios where one pump is inactive ($1 \times$ TMP).

VII. DISCUSSION

These calculations demonstrate that the overall macroscopic shielding thickness ultimately dominates downstream dose-rate attenuation, rendering the localized prompt-radiation benefits of high-density materials such as Densimet marginal at larger distances. Moreover, the simulated residual dose rates represent a conservative worst-case scenario. In practical operation, switching to beam-pass mode rotates the highly activated faces of the dynamic blocks into the surrounding static structure. This self-shielding effect, combined with the physical inaccessibility of the immediate upstream region, ensures safe personnel access to the FHF1 experimental area within approximately 1 day after beam-dumping operations, independent of the core absorber material.

Although the Densimet configuration offers modestly improved attenuation near the interaction region, this gain is outweighed by its significantly higher density, material and machining costs, and mechanical load (see Table I). Consequently, an iron-based configuration provides a fully practical, mechanically manageable, and cost-efficient solution that satisfies all radiation-protection criteria. These results confirm that the proposed compact switchable beam-dump concept meets operational safety requirements while preserving simplicity and affordability.

VIII. CONCLUSION AND OUTLOOK

The conceptual design of a compact switchable beam-dump assembly for high-intensity heavy-ion facilities such as the Super-FRS at FAIR has been presented. By integrating radiation shielding, vacuum integrity, and mechanical actuation within the existing volume of a modular shielding wall, the proposed system eliminates the spatial constraints and downtime associated with conventional static beam dumps. This architecture represents a first-of-a-kind engineering solution for switchable shielding. Direct integration of the beam dump into the facility's structural shielding optimizes experimental floor space, minimizes transition downtime, and increases overall throughput.

FLUKA simulations of the iron and Densimet configurations confirm that both absorber designs meet stringent radiation-safety requirements with a substantial margin: prompt dose rates in the downstream area remain well below 3 μSv/h, controlled access to the upstream area is achievable within approximately 1 week, and beamline-compatible vacuum pressures are maintained under normal and single-pump-failure conditions. The present study is, however, limited to conceptual-level analysis. Key aspects not yet addressed include detailed structural and fatigue analysis of the gear train and turntable under long-term irradiation, qualification of vacuum-compatible bearing and lubricant solutions under the expected radiation environment, and experimental validation of the shielding performance. These will be addressed in the engineering design study currently underway, which includes mechanical prototyping, radiation surveys, and system-level testing, with system realization anticipated in early 2027.

Beyond the Super-FRS, this switchable shielding concept offers potential for broader applications in nuclear research and radioisotope production facilities where space and maintainability are critical. Its modularity and scalability support diverse multimaterial configurations. One promising extension is a radiation load-lock mechanism, realized by employing two such systems with a 90° phase difference to maintain continuous shielding during transitions and prevent line-of-sight leakage. These principles may also prove relevant in space-based research or extraterrestrial habitat design, where efficient management of shielding mass and volume is essential.

ACKNOWLEDGMENTS

The authors would like to thank Dennis Gassmann and Torsten Radon for their valuable contributions and guidance on radiation-safety aspects. We are also grateful to Petra Hofmann, Martin Mikulla, Robin Jürgen Similon, and Alexander Bergmann and Stefan Kreis for the technical discussions and input regarding the civil-construction aspects of the project. Furthermore, we acknowledge Helena Albers, Haik Simon, Martin Winkler, and Stephan Reimann for their support at the organizational level in establishing the concept as a potential candidate for the Super-FRS radiation-safety framework.

S. P. conceived the original idea and design concept, led the project, and prepared the manuscript. N. K. created the 3D models, carried out the vacuum simulations, and contributed to the radiation-safety analysis, data visualization, conceptual refinement, and manuscript preparation. E. K. performed the FLUKA simulations and contributed to the interpretation of the radiation-safety analysis and to the manuscript. D. J. M. contributed to initial concept development, interpretation of the results, and critical manuscript revision.

DATA AVAILABILITY

There are no publicly available research data or software supporting this manuscript. Requests for further information or data should be sent to the authors.

APPENDIX A: REALISTIC AND SIMPLIFIED FLUKA SIMULATION GEOMETRIES

This appendix presents the geometries used in the FLUKA radiation-safety simulations of the switchable beam-dump system (Figs. 10 and 11). For each case, the top panel displays the realistic engineering layout, and

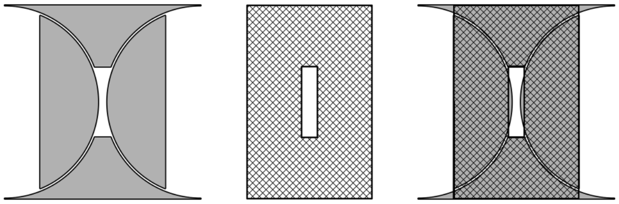

FIG. 9. Comparison of the mechanical shielding geometry and the simplified radiation-transport model. Left: Realistic mechanical geometry of the switchable shielding block. Middle: Simplified geometry used in the Monte Carlo model. Right: Overlay of both geometries.

the bottom panel shows the corresponding simplified FLUKA model.

Because highly detailed mechanical models increase computational cost without significantly altering particle transport, the geometries were simplified to optimize the Monte Carlo calculations. These structural simplifications reduce particle tracking time while strictly preserving the mass distribution, scattering behavior, and overall shielding efficacy of the original design.

The simplified geometry was constructed conservatively. As shown in Fig. 9, the realistic curved gap between the movable shielding elements was replaced by a rectangular aperture. This aperture is larger and more direct than the realistic gap and therefore overestimates the possible radiation streaming path. In addition, the 5 cm gaps assumed around the system are larger than the actual configuration, providing an additional safety margin for the calculated dose rates.

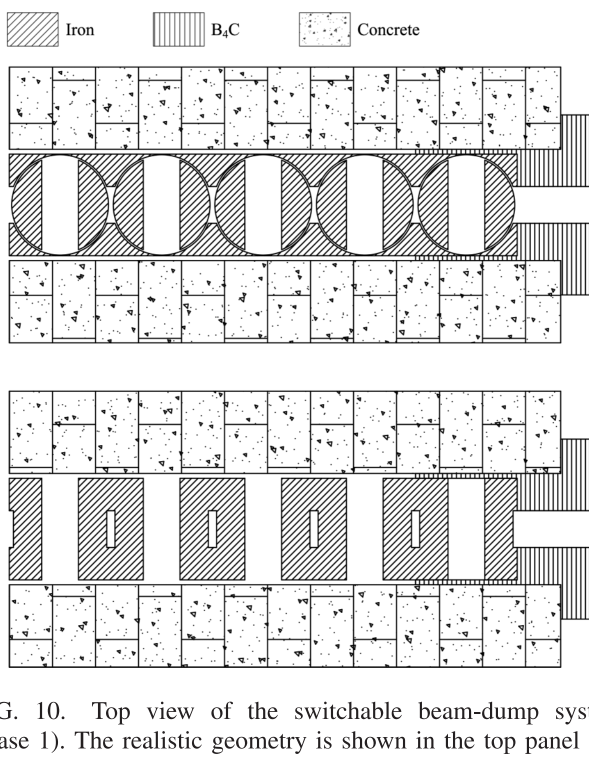

FIG. 10. Top view of the switchable beam-dump system (Case 1). The realistic geometry is shown in the top panel and the simplified FLUKA simulation geometry in the bottom panel.

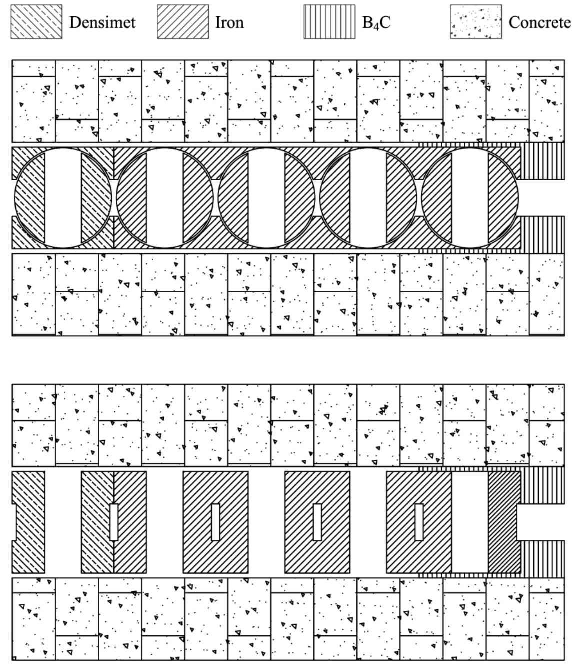

FIG. 11. Top view of the switchable beam-dump system (Case 2). The realistic geometry is shown in the top panel and the simplified FLUKA simulation geometry in the bottom panel.

Small mechanical details, curved surfaces, rails, screws, and auxiliary support features were not credited as shielding material. Their omission avoids an artificial reduction of the calculated dose rates due to minor components. The simplified model therefore preserves the relevant shielding thickness and scattering conditions while giving a conservative estimate of the radiation transport outside the switchable shielding unit.

APPENDIX B: RESIDUAL-DOSE REDUCTION USING MOBILE LEAD SHIELDING

To expedite access to the experimental area, the implementation of mobile lead shielding was evaluated. For the purpose of estimating the effectiveness of portable lead shielding, the characteristic mean gamma energy of the residual radiation field can be approximated to lie in the range of 0.8–1.3 MeV, as discussed above. Using the mass attenuation coefficient of gamma rays in lead, the corresponding TVL is approximately 3.45 cm [27]. A shielding thickness of 7 cm reduces the residual dose rate to below 0.5 $\mu Sv/h$. These analytical estimates are in good agreement with FLUKA simulations, as shown in Fig. 12. A thickness of 4.25 cm lead shielding is sufficient to achieve the target dose rate of $< 3\ \mu Sv/h$ for safe personnel access.

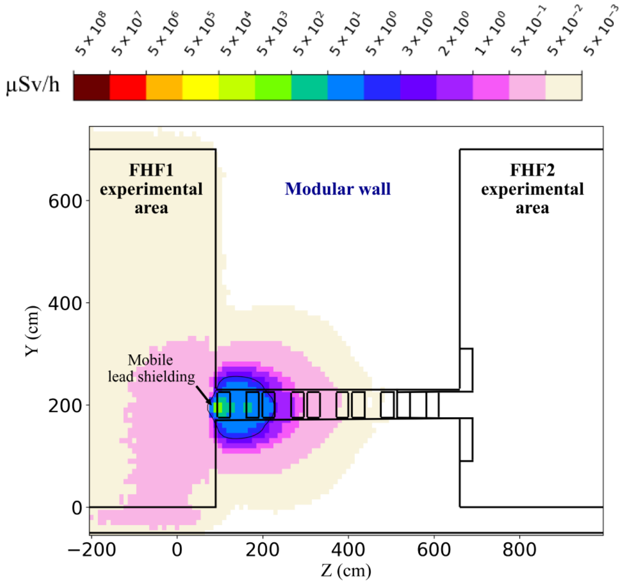

FIG. 12. Residual dose-rate distribution (side view, $y-z$ plane at $x=0$) for Case 1 with 7 cm lead shielding at the entrance, shown after a 1-day cooling period.

APPENDIX C: DOMINANT RADIONUCLIDES IN TARGET MATERIALS

Table III presents the dominant radionuclides produced in iron and tungsten (Densimet), as obtained from the FLUKA simulations. To highlight the most significant radiation sources, the table includes only those isotopes contributing $\geq 1\%$ to the total dose and possessing gamma energies $E_\gamma > 100$ keV. Because many of these radionuclides exhibit complex decay schemes, only the single most dominant, representative gamma-ray energy line is listed for each isotope.

The fractional dose contributions were calculated under the conservative assumption that all listed radionuclides are concentrated at a single point source, with the dose evaluated in air at a distance of 1 m [31]. The specific nuclides detailed in this appendix represent the primary drivers of the residual dose-rate distributions previously shown in Figs. 6 and 12.

TABLE III. Dominant radionuclides, their half-lives $T_{1/2}$, and gamma contributions for iron and tungsten at different cooling times. One representative gamma energy is listed for each radionuclide.

Iron

1 day				1 week				1 month			
Nuclide	E_γ (keV)	$T_{1/2}$ (days)	% dose	Nuclide	E_γ (keV)	$T_{1/2}$ (days)	% dose	Nuclide	E_γ (keV)	$T_{1/2}$ (days)	% dose
^{48}V	1312	15.97	44.41%	^{48}V	1312	15.97	53.68%	^{48}V	1312	15.97	54.47%
^{52}Mn	1434	5.59	37.89%	^{52}Mn	1434	5.59	28.20%	^{54}Mn	834	312.5	24.51%
^{54}Mn	834	312.5	6.05%	^{54}Mn	834	312.5	9.32%	^{46}Sc	1120	83.8	7.63%
^{46}Sc	1120	83.8	2.25%	^{46}Sc	1120	83.8	3.36%	^{56}Co	1238	77.3	5.58%
^{44}Sc	1157	0.17	2.03%	^{56}Co	1238	77.3	2.50%	^{52}Mn	1434	5.59	4.49%
^{56}Co	1238	77.3	1.68%	^{51}Cr	320	27.7	1.45%	^{51}Cr	320	27.7	2.24%
^{48}Sc	1312	1.82	1.31%								
^{51}Cr	320	27.7	1.07%								

Tungsten (Densimet)

1 day				1 week				1 month			
Nuclide	E_γ (keV)	$T_{1/2}$ (days)	% dose	Nuclide	E_γ (keV)	$T_{1/2}$ (days)	% dose	Nuclide	E_γ (keV)	$T_{1/2}$ (days)	% dose
^{187}W	685	0.99	52.55%	^{171}Lu	739	8.24	16.05%	^{175}Hf	343	70.0	17.15%
^{170}Lu	1280	2.01	8.32%	^{175}Hf	343	70.0	9.18%	^{58}Co	810	70.9	16.22%
^{176}Ta	1159	0.34	5.25%	^{58}Co	810	70.9	8.66%	^{182}Ta	1221	114.4	12.88%
^{171}Lu	739	8.24	4.13%	^{170}Lu	1280	2.01	7.86%	^{56}Co	1238	77.3	7.67%
^{166}Tm	779	0.32	4.00%	^{182}Ta	1221	114.4	6.31%	^{169}Yb	197	32.0	6.57%
^{169}Lu	961	1.42	2.51%	^{187}W	685	0.99	5.20%	^{172}Lu	1093	6.70	6.51%
^{175}Ta	348	0.44	2.42%	^{166}Tm	779	0.32	4.44%	^{171}Lu	739	8.24	5.46%
^{173}Hf	123	0.98	2.36%	^{172}Lu	1093	6.70	4.37%	^{146}Eu	747	4.61	4.30%
^{175}Hf	343	70.0	1.53%	^{56}Co	1238	77.3	3.99%	^{48}V	1312	15.97	1.81%
^{177}Ta	113	2.35	1.51%	^{183}Ta	246	5.10	3.44%	^{178}W	426	21.6	1.73%
^{58}Co	810	70.9	1.45%	^{146}Eu	747	4.61	2.61%	^{184}Re	903	35.4	1.08%
^{183}Ta	246	5.10	1.23%	^{48}V	1312	15.97	2.09%	^{173}Lu	272	500.4	1.00%
^{182}Ta	1221	114.4	1.03%								

[a]The representative 426-keV photon is emitted by the short-lived daughter ^{178}Ta in the ^{178}W decay chain

[1] D. Baillard, E. Grenier-Boley, M. Dole, F. Deslande, R. Froeschl, T. Lorenzon, P. Moyret, R. Peron, A. Pilan Zanoni, C. Sharp, M. Timmins, and M. Calviani, Design, development, and construction of the new beam stoppers for CERN's injector complex, arXiv:2408.01074.

[2] A. P. Zanoni, J. A. B. Monago, E. Grenier-Boley, M. Calviani, and V. Vlachoudis, Characterization and core renovation of beam stoppers for personnel safety, J. Instrum. **14**, T01011 (2019).

[3] C. Kharoua, P. Sabbagh, P. Nilsson, F. Mezei, F. Plewinski, E. Noah, P. Sievers, L. Zanini, A. Takibayev, S. Kecskes *et al.*, The rotating tungsten helium cooled target (Rotheta) concept, in *Proc. International Collaboration on Advanced Neutron Sources* (Centro Atomico Bariloche, Argentina, 2013).

[4] N. Tahir, M. Winkler, J. Kojouharova, P. Roussel-Chomaz, V. Chishkine, H. Geissel, D. Hoffmann, B. Kindler, F. Landre-Pellemoine, B. Lommel *et al.*, High-power production targets for the super-FRS using a fast extraction scheme, Nucl. Instrum. Methods Phys. Res., Sect. B **204**, 282 (2003).

[5] S. Péraire and P. R. Sala, Beam dumps and beam stoppers for LHC and CNGS transfer lines, Tech. Rep. CERN-LHC-PROJECT-REPORT-465, CERN, Geneva, Switzerland, 2001.

[6] V. Kain, R. Esposito, M. Meddahi, M. Fraser, B. Goddard, F. Velotti, A. Perillo Marcone, and G. Steele, Upgrades to the SPS-to-LHC transfer line beam stoppers for the LHC high-luminosity era, in *Proceedings of the 7th International Particle Accelerator Conference (IPAC'16)* (JACoW, Busan, Korea, 2016), pp. 1367–1370.

[7] H. Geissel, H. Weick, M. Winkler, G. Münzenberg, V. Chichkine, M. Yavor, T. Aumann, K. Behr, M. Böhmer, A. Brünle *et al.*, The Super-FRS project at GSI, Nucl. Instrum. Methods Phys. Res., Sect. B **204**, 71 (2003).

[8] S. Reimann, H. Albers, R. W. Assmann, P. Gasik, O. Geithner, F. Hagenbuck, A. Herlert, P. Hofmann, V. Kamerdzhiev, M. Kauschke, H. Kollmus, S. Pietri, N. Pyka, T. Radon, C. Schroeder, S. Schwarz, H. Simon, P. Spiller, and K. Vogt, FAIR commissioning—towards first science, in *Proceedings of the 16th International Particle Accelerator Conference* (JACOW Publishing, Taipei, Taiwan, 2025).

[9] N. Kalantar-Nayestanaki and A. Bruce, NUSTAR: Nuclear structure astrophysics and reactions at FAIR, Nucl. Phys. News **28**, 5 (2018).

[10] A. Fertman, E. Mustafin, R. Hinca, I. Strašík, M. Pavlovič, D. Schardt, N. Sobolevskiy, A. Golubev, B. Sharkov, G. Fehrenbacher *et al.*, First results of an experimental study of the residual activity induced by high-energy uranium ions in steel and copper, Nucl. Instrum. Methods Phys. Res., Sect. B **260**, 579 (2007).

[11] I. Strašík, E. Mustafin, and M. Pavlovič, Residual activity induced by heavy ions and beam-loss criteria for heavy-ion accelerators, Phys. Rev. Spec. Top. Accel. Beams **13**, 071004 (2010).

[12] International Atomic Energy Agency, Decommissioning of particle accelerators, Tech. Rep. NW-T-2.9, IAEA, Vienna, 2020.

[13] International Commission on Radiological Protection, *Conversion Coefficients for Use in Radiological Protection Against External Radiation*, ICRP Publication 74 (Pergamon Press, Oxford, United Kingdom, 1996).

[14] B. R. Evans, J. Lian, and W. Ji, Evaluation of shielding performance for newly developed composite materials, Ann. Nucl. Energy **116**, 1 (2018).

[15] J. R. Jones, Lubrication, friction and wear: Space vehicle design criteria (Structures), Tech. Rep. NASA-SP-8063, NASA, 1971.

[16] P. A. Shakhmatov, K. H. Kim, and S. G. Yoon, Solid lubricants and coatings for aerospace and vacuum applications, in *Tribology in Space Applications*, edited by J. R. Moraes, K. Tanaka, H. Tsuchiya, T. Matsuzaki, and S. Umeda (Springer, New York, 2017), pp. 253–276.

[17] A. Erdemir and O. L. Eryilmaz, Tribological performance of DLC coatings in ultrahigh vacuum, J. Vac. Sci. Technol., A **35**, 030601 (2017).

[18] Federal Ministry for the Environment, Nature conservation, nuclear safety and consumer protection (BMUV), German radiation protection ordinance (strahlenschutzverordnung, strlschv), German Federal Law Gazette I (2018), bGBl. I S. 2034; last amended 18 July 2023.,

[19] S. H. Rokni, A. Fassò, and J.-C. Liu, Operational radiation protection program at high-energy accelerator facilities, Radiat. Prot. Dosim. **137**, 3 (2009).

[20] Safety of machinery—safety-related parts of control systems—part 1: General principles for design (2015).

[21] Functional safety of electrical/electronic/programmable electronic safety-related systems (2010). parts 1-7.

[22] T. T. Böhlen, F. Cerutti, M. Chin, A. Fassò, A. Ferrari, P. Ortega, A. Mairani, P. Sala, G. Smirnov, and V. Vlachoudis, The FLUKA code: Developments and challenges for high energy and medical applications, Nucl. Data Sheets **120**, 211 (2014).

[23] A. Ferrari, P. R. Sala, A. Fassò, and J. Ranft, FLUKA: A multi-particle transport code, CERN-2005-10, INFN/TC 05/11, SLAC-R-773 (2005).

[24] F. Ballarini *et al.*, The FLUKA code: Overview and new developments, EPJ Nucl. Sci. Technol. **10**, 16 (2024).

[25] V. Vlachoudis, FLAIR: A powerful but user friendly graphical interface for FLUKA, in *Proc. Int. Conf. on Mathematics, Computational Methods & Reactor Physics (M&C2009)* (Saratoga Springs, New York, 2009).

[26] A. Ferrari and M. Pelliccioni, Fluence to dose equivalent conversion data and effective quality factors for high energy neutrons, Rad. Prot. Dosimetry **76**, 215 (1998).

[27] J. H. Hubbell and S. M. Seltzer, Tables of X-ray mass attenuation coefficients and mass energy-absorption coefficients, National Institute of Standards and Technology (NIST), 1995, https://physics.nist.gov/PhysRefData/ XrayMassCoef/, accessed: 2026-03-18.

[28] E. Kozlova, I. Strasik, A. Fertman, E. Mustafin, T. Radon, R. Hinca, M. Pavlovic, G. Fehrenbacher, H. Geissel, A. Golubev, H. Iwase, and D. Schardt, Benchmark test of the FLUKA Monte Carlo code for residual production with 500 and 950 MeV/u uranium beams on copper and stainless steel targets, Nucl. Technol. **168**, 747 (2017).

[29] R. Froeschl, The DORIAN code for the prediction and analysis of residual dose rates due to accelerator radiation induced activation, Tech. Rep., CERN, Geneva, 2013.

[30] M. Ady and R. Kersevan, Recent developments of Monte-Carlo codes MolFlow+ and SynRad+, in *Proceedings of the 10th International Particle Accelerator Conference (IPAC'19)* (JACoW, Melbourne, Australia, 2019).

[31] N. Petoussi, M. Zankl, G. Fehrenbacher, and G. Drexler, Dose distributions in the ICRU sphere for monoenergetic photons and electrons and for ca. 800 radionuclides, Tech. Rep. GSF Report 7/93, GSF—Forschungszentrum für Umwelt und Gesundheit, Neuherberg, Germany, 1993.